PHYSICAL REVIEW D **82,** 125037 (2010)

Properties of charged rotating electroweak sphaleron-antisphaleron systems

Rustam Ibadov

Department of Theoretical Physics and Computer Science, Samarkand State University, Samarkand, Uzbekistan

Burkhard Kleihaus, Jutta Kunz, and Michael Leissner

Institut für Physik, Universität Oldenburg, D-26111 Oldenburg, Germany

(Received 26 October 2010; published 28 December 2010)

We perform a systematic study of stationary sphaleron-antisphaleron systems of Weinberg-Salam theory at the physical value of the weak mixing angle. These systems include rotating sphaleron-antisphaleron pairs, chains, and vortex rings. We show that the angular momentum of these solutions is proportional to their electric charge. We study the dependence of their energy and magnetic moment on their angular momentum. We also investigate the influence of their angular momentum on their local properties, in particular, on their energy density and on the node structure of their Higgs field configuration. Furthermore, we discuss the equilibrium condition for these solutions.

DOI: 10.1103/PhysRevD.82.125037 PACS numbers: 11.15.−q, 11.27.+d, 12.15.−y

I. INTRODUCTION

It came as a surprise when 't Hooft [1] observed in 1976 that because of the Adler-Bell-Jackiw anomaly, the standard model does not absolutely conserve baryon and lepton number. The process 't Hooft considered was spontaneous fermion number violation due to instanton induced transitions. Later, Ringwald [2] argued that such tunneling transitions between topologically distinct vacua might be observable at high energies at future accelerators.

The presence of baryon and lepton number violating processes in the standard model was considered by Manton [3] from another point of view. He investigated the topological structure of the configuration space of Weinberg-Salam theory and found the existence of noncontractible loops. From these he predicted the existence of a static, unstable solution of the bosonic field equations, representing the top of the energy barrier between topologically distinct vacua. Because of its instability this classical electroweak solution was termed sphaleron by Klinkhamer and Manton [4].

At finite temperature the energy barrier between topologically distinct vacua can be overcome due to thermal fluctuations of the fields, and baryon number violating vacuum to vacuum transitions involving changes of baryon and lepton number can occur. The rate for such baryon number violating processes is largely determined by a Boltzmann factor, containing the height of the barrier at a given temperature and thus the energy of the sphaleron [5–8]. Entailing baryon number violating processes, the sphaleron itself carries baryon number $Q_{\mathrm{B}} = 1/2$ [4].

The energy of the sphaleron increases with increasing Higgs mass and ranges roughly between 7 and 13 TeV [4,9,10]. The energy is that high, since its scale is not set by M_W but by M_W/α_{w}. For the physical value of the weak mixing angle the sphaleron energy is only slightly decreased as compared to the vanishing mixing angle [11,12]. However, the configuration is no longer spherically symmetric, and retains only axial symmetry. At the same time, one finds a large value for the magnetic dipole moment of the sphaleron, $\mu_{\mathrm{S}} \approx 1.8e/(\alpha_{\mathrm{w}} M_W)$ [4,11,12].

Whereas the static electroweak sphaleron does not carry electric charge, it was argued before [13] and demonstrated recently in nonperturbative studies [14,15] that the addition of electric charge leads to a nonvanishing Poynting vector and thus a finite angular momentum density of the system. Consequently, a branch of electrically charged sphalerons arises that carry, at the same time, angular momentum. In particular, their angular momentum and charge are proportional. Since these charged sphalerons carry nonvanishing baryon number as well, they can also entail baryon number violating processes.

Besides the sphaleron, the nontrivial topology of the configuration space of Weinberg-Salam theory gives rise to further unstable classical solutions. A superposition of n sphalerons, for instance, can lead to static axially symmetric solutions, multisphalerons, which carry baryon number $Q_{\mathrm{B}} = n/2$ and whose energy density is toruslike [16–18]. A superposition of a sphaleron and an antisphaleron, on the other hand, can give rise to a bound sphaleron-antisphaleron system, in which a sphaleron and an antisphaleron are located at an equilibrium distance on the symmetry axis [19–21]. Such a sphaleron-antisphaleron pair has vanishing baryon number, $Q_{\mathrm{B}} = 0$, since the antisphaleron carries $Q_{\mathrm{B}} = -1/2$. The sphaleron-antisphaleron pair therefore does not mediate baryon number violating processes.

Recently, the sphaleron-antisphaleron pair solutions have been generalized, leading to sphaleron-antisphaleron chains, where m sphalerons and antisphalerons are located on the symmetry axis in static equilibrium [22], in close analogy to the monopole-antimonopole chains encountered in the Georgi-Glashow model [23]. When systems of multisphalerons and multiantisphalerons are considered, instead of the anticipated pairs and chains a new type of

solutions arises, when $n \geq 3$ [22]. In these vortex ring solutions the Higgs field vanishes not (only) on isolated points on the symmetry axis but (also) on one or more rings, centered around the symmetry axis [24,25].

In this paper we perform a systematic study of multisphalerons and sphaleron-antisphaleron systems endowed with electric charge [26]. As for the simple sphaleron, the nonvanishing Poynting vector leads to a finite angular momentum density for these configurations. Thus branches of rotating electrically charged sphaleron-antisphaleron systems emerge from the respective static electrically neutral configurations. We construct these solutions explicitly for $m, n \leq 6$ and discuss their properties. We demonstrate that the angular momentum and the electric charge of the solutions are proportional [14,22,26,27].

In Sec. II we present the action, the Ansatz for the stationary axially symmetric configurations, and the boundary conditions. We then consider the relevant physical properties and, in particular, derive the linear relation between angular momentum and electric charge. We present and discuss the numerical results in Sec. III. These include global properties of the solutions, such as their energy, their angular momentum, their charge, and their magnetic moments, but also local properties, such as their energy density, their angular momentum density, and the modulus of their Higgs field. Moreover, we discuss the equilibrium condition for these solutions. We give our conclusions in Sec. IV.

II. ACTION, ANSATZ, AND PROPERTIES

A. Weinberg-Salam Lagrangian

We consider the bosonic sector of Weinberg-Salam theory,

$$\mathcal{L} = -\frac{1}{2}\,\mathrm{Tr}(F_{\mu\nu}F^{\mu\nu}) - \frac{1}{4}f_{\mu\nu}f^{\mu\nu} - (D_\mu\Phi)^\dagger(D^\mu\Phi) - \lambda\left(\Phi^\dagger\Phi - \frac{\upsilon^2}{2}\right)^2, \tag{1}$$

with the $su(2)$ field strength tensor

$$F_{\mu\nu} = \partial_\mu V_\nu - \partial_\nu V_\mu + ig[V_\mu, V_\nu], \tag{2}$$

the $su(2)$ gauge potential $V_\mu = V_\mu^a \tau_a/2$, the $u(1)$ field strength tensor

$$f_{\mu\nu} = \partial_\mu A_\nu - \partial_\nu A_\mu, \tag{3}$$

and the covariant derivative of the Higgs field

$$D_\mu\Phi = \left(\partial_\mu + igV_\mu + i\frac{g'}{2}A_\mu\right)\Phi, \tag{4}$$

where g and g' denote the $SU(2)$ and $U(1)$ gauge coupling constants, respectively, λ denotes the strength of the Higgs self-interaction and υ the norm of the vacuum expectation value of the Higgs field.

The gauge symmetry is spontaneously broken due to the nonvanishing vacuum expectation value of the Higgs field

$$\langle\Phi\rangle = \frac{\upsilon}{\sqrt{2}}\begin{pmatrix}0\\1\end{pmatrix}, \tag{5}$$

leading to the boson masses

$$M_W = \frac{1}{2}g\upsilon, \qquad M_Z = \frac{1}{2}\sqrt{(g^2+g'^2)}\upsilon, \qquad M_H = \upsilon\sqrt{2\lambda}. \tag{6}$$

$\tan\theta_\mathrm{w} = g'/g$ determines the weak mixing angle θ_w, defining the electric charge $e = g\sin\theta_\mathrm{w}$. We also denote the weak fine-structure constant $\alpha_\mathrm{W} = g^2/4\pi$.

B. Stationary axially symmetric Ansatz

To obtain stationary rotating solutions of the bosonic sector of Weinberg-Salam theory, we employ the time-independent axially symmetric Ansatz

$$V_\mu dx^\mu = \left(B_1\frac{\tau_r^{(n,m)}}{2g} + B_2\frac{\tau_\theta^{(n,m)}}{2g}\right)dt - n\sin\theta\left(H_3\frac{\tau_r^{(n,m)}}{2g} + H_4\frac{\tau_\theta^{(n,m)}}{2g}\right)d\varphi + \left(\frac{H_1}{r}dr + (1-H_2)d\theta\right)\frac{\tau_\varphi^{(n)}}{2g}, \tag{7}$$

$$A_\mu dx^\mu = (a_1 dt + a_2\sin^2\theta d\varphi)/g', \tag{8}$$

and

$$\Phi = i(\phi_1\tau_r^{(n,m)} + \phi_2\tau_\theta^{(n,m)})\frac{\upsilon}{\sqrt{2}}\begin{pmatrix}0\\1\end{pmatrix}, \tag{9}$$

where

$$\tau_r^{(n,m)} = \sin m\theta(\cos n\varphi\,\tau_x + \sin n\varphi\,\tau_y) + \cos m\theta\,\tau_z,$$
$$\tau_\theta^{(n,m)} = \cos m\theta(\cos n\varphi\,\tau_x + \sin n\varphi\,\tau_y) - \sin m\theta\,\tau_z,$$
$$\tau_\varphi^{(n)} = (-\sin n\varphi\,\tau_x + \cos n\varphi\,\tau_y),$$

n and m are integers, and τ_x, τ_y, and τ_z denote the Pauli matrices.

The two integers n and m determine the type of configuration that is put into rotation. For $n = m = 1$ the solutions correspond to rotating sphalerons. Rotating multisphaleron configurations arise for $n > 1$ and $m = 1$. For $n = 1$ and $m > 1$ rotating sphaleron-antisphaleron pairs ($m = 2$) or sphaleron-antisphaleron chains arise, and for $n \geq 3$ rotating vortex ring solutions are obtained.

The ten functions $B_1, B_2, H_1, \ldots, H_4, a_1, a_2, \phi_1$, and ϕ_2 depend on r and θ only. With this Ansatz the full set of field equations reduces to a system of ten coupled partial differential equations in the independent variables r and θ. A residual $U(1)$ gauge degree of freedom is fixed by the condition $r\partial_r H_1 - \partial_\theta H_2 = 0$ [11].

C. Boundary conditions

Requiring regularity and finite energy, we impose for odd m configurations the boundary conditions

$$
\begin{aligned}
&r=0: B_1 \sin m\theta + B_2 \cos m\theta = 0, \quad \partial_r (B_1 \cos m\theta - B_2 \sin m\theta) = 0, \quad H_1 = H_3 = H_4 = 0, \quad H_2 = 1, \\
&\qquad \partial_r a_1 = 0, \quad a_2 = 0, \quad \phi_1 = 0, \quad \phi_2 = 0 \\
&r \to \infty: B_1 = \gamma \cos m\theta, \quad B_2 = \gamma \sin m\theta, \quad H_1 = H_3 = 0, \quad H_2 = 1 - 2m, \quad H_4 = \frac{2 \sin m\theta}{\sin\theta}, \\
&\qquad a_1 = \gamma, \quad a_2 = 0, \quad \phi_1 = 1, \quad \phi_2 = 0, \quad \text{where } \gamma = \text{const.} \\
&\theta = 0: \partial_\theta B_1 = 0, \quad B_2 = 0, \quad H_1 = H_3 = 0, \quad \partial_\theta H_2 = \partial_\theta H_4 = 0, \quad \partial_\theta a_1 = \partial_\theta a_2 = 0, \quad \partial_\theta \phi_1 = 0, \quad \phi_2 = 0, \qquad (10)
\end{aligned}
$$

where the latter hold also at $\theta = \pi/2$, except for $B_1 = 0$ and $\partial_\theta B_2 = 0$. For even m configurations the same set of boundary conditions holds except for

$$
\begin{aligned}
&r = 0: \ \phi_1 \sin m\theta + \phi_2 \cos m\theta = 0, \\
&\qquad \partial_r (\phi_1 \cos m\theta - \phi_2 \sin m\theta) = 0, \\
&\theta = \pi/2: \ \partial_\theta B_1 = 0, \quad B_2 = 0, \\
&\qquad \partial_\theta H_3 = 0, \quad H_4 = 0. \qquad (11)
\end{aligned}
$$

D. Mass, angular momentum, and charge

We now address the global charges of the sphaleron-antisphaleron systems, their energy, their angular momentum, their electric charge, and their baryon number. The energy E and angular momentum J are defined in terms of volume integrals of the respective components of the energy-momentum tensor. The energy is obtained from

$$
E = -\int T_t^t d^3 r, \qquad (12)
$$

while the angular momentum

$$
\begin{aligned}
J &= \int T_\varphi^t d^3 r \\
&= \int [2\,\mathrm{Tr}(F^{t\mu} F_{\varphi\mu}) + f^{t\mu} f_{\varphi\mu} + 2(D^t \Phi)^\dagger (D_\varphi \Phi)] d^3 r \qquad (13)
\end{aligned}
$$

can be reexpressed with the help of the equations of motion and the symmetry properties of the Ansatz [27–30] as a surface integral at spatial infinity,

$$
\begin{aligned}
J = \int_{S_2} \Big\{ &2\,\mathrm{Tr}\Big(\Big(V_\varphi - \frac{n\tau_z}{2g}\Big) F^{rt}\Big) \\
&+ \Big(A_\varphi - \frac{n}{g'}\Big) f^{rt} \Big\} r^2 \sin\theta d\theta d\varphi. \qquad (14)
\end{aligned}
$$

The power law falloff of the $U(1)$ field of a charged solution allows for a finite flux integral at infinity and thus a finite angular momentum. Insertion of the asymptotic expansion for the $U(1)$ field,

$$
a_1 = \gamma - \frac{\chi}{r} + O\Big(\frac{1}{r^2}\Big), \qquad a_2 = \frac{\zeta}{r} + O\Big(\frac{1}{r^2}\Big), \qquad (15)
$$

and of the analogous expansion for the $SU(2)$ fields then yields for the angular momentum

$$
\frac{J}{4\pi} = \frac{n\chi}{g^2} + \frac{n\chi}{g'^2} = \frac{n\chi}{g^2 \sin^2\theta_\mathrm{w}} = \frac{n\chi}{e^2}. \qquad (16)
$$

The field strength tensor $\mathcal{F}_{\mu\nu}$ of the electromagnetic field $\mathcal{A}_\mu$,

$$
\mathcal{A}_\mu = \sin\theta_\mathrm{w} V_\mu^3 + \cos\theta_\mathrm{w} A_\mu, \qquad (17)
$$

as given in a gauge where the Higgs field asymptotically tends to Eq. (5), then defines the electric charge $\mathcal{Q}$,

$$
\begin{aligned}
\mathcal{Q} &= \int_{S_2} {}^*\mathcal{F}_{\theta\varphi} d\theta d\varphi = 4\pi \Big\{ \frac{\sin\theta_\mathrm{w} \chi}{g} + \frac{\cos\theta_\mathrm{w} \chi}{g'} \Big\} \\
&= 4\pi \frac{\chi}{e}, \qquad (18)
\end{aligned}
$$

where the integral is evaluated at spatial infinity. Comparison of Eqs. (16) and (18) then yields a linear relation between the angular momentum J and the electric charge $\mathcal{Q}$ [14,15],

$$
J = \frac{n\mathcal{Q}}{e}. \qquad (19)
$$

This relation corresponds to the relation for monopole-antimonopole systems without magnetic charge [31]. The magnetic moment μ is obtained from the asymptotic expansion Eq. (15), analogously to the electric charge,

$$
\mu = \frac{4\pi\zeta}{e}. \qquad (20)
$$

E. Baryon number

Addressing finally the baryon number Q_B, its rate of change is given by

$$
\begin{aligned}
\frac{dQ_\mathrm{B}}{dt} &= \int d^3 r \partial_t j_\mathrm{B}^0 \\
&= \int d^3 r \Big[\vec{\nabla} \cdot \vec{j}_\mathrm{B} + \frac{1}{32\pi^2} \epsilon^{\mu\nu\rho\sigma} \Big\{ g^2 \mathrm{Tr}(F_{\mu\nu} F_{\rho\sigma}) \\
&\quad + \frac{1}{2} g'^2 f_{\mu\nu} f_{\rho\sigma} \Big\} \Big]. \qquad (21)
\end{aligned}
$$

Starting at time $t = -\infty$ at the vacuum with $Q_\mathrm{B} = 0$, one obtains the baryon number of a sphaleron solution at time $t = t_0$ [4],

$$
Q_\mathrm{B} = \int_{-\infty}^{t_0} dt \int_S \vec{K} \cdot d\vec{S} + \int_{t=t_0} d^3 r K^0, \qquad (22)
$$

where the $\vec{\nabla}\cdot\vec{j}_{\rm B}$ term is neglected, and the anomaly term is reexpressed in terms of the Chern-Simons current

$$K^{\mu}=\frac{1}{16\pi^2}\,\varepsilon^{\mu\nu\rho\sigma}\Big\{g^2{\rm Tr}\Big(F_{\nu\rho}V_{\sigma}-\frac{2}{3}igV_{\nu}V_{\rho}V_{\sigma}\Big)+\frac{1}{2}g'^2f_{\nu\rho}A_{\sigma}\Big\}. \tag{23}$$

In a gauge, where

$$V_{\mu}\rightarrow\frac{i}{g}\partial_{\mu}\hat{U}\hat{U}^{\dagger},\qquad \hat{U}(\infty)=1, \tag{24}$$

$\vec{K}$ vanishes at infinity. Subject to the above Ansatz and boundary conditions the baryon charge of the sphaleron solution [17,32] is then

$$Q_{\rm B}=\int_{t=t_0}d^3rK^0=\frac{n(1-(-1)^m)}{4}. \tag{25}$$

III. RESULTS AND DISCUSSION

A. Numerical technique

We have solved the set of ten coupled nonlinear elliptic partial differential equations numerically, subject to the above boundary conditions. We have employed the compactified dimensionless coordinate

$$x=\tilde{r}/(1+\tilde{r}),\qquad \tilde{r}=g\upsilon r, \tag{26}$$

instead of $\tilde{r}$, to map spatial infinity to the finite value $x=1$.

The numerical calculations are performed with the help of the program FIDISOL [33]. The equations are discretized on a nonequidistant grid in x and θ. Typical grids used have sizes in the range 100×60 to 120×80, covering the integration region $0\leq x\leq 1$ and $0\leq\theta\leq\pi/2$.

The numerical method is based on the Newton-Raphson method, an iterative procedure to find a good approximation to the exact solution. The iteration stops when the Newton residual is smaller than a prescribed tolerance. Thus it is essential to have a good first guess, to start the iteration procedure. Our strategy therefore is to use a known solution as a guess and then vary some parameter to obtain the next solution.

Restricting to $M_H=M_W$, and employing the physical value for the mixing angle $\theta_{\rm w}$, we have performed a systematic study of the rotating sphaleron-antisphaleron systems with $1\leq m\leq 6$ and $1\leq n\leq 6$. We have also obtained samples of solutions for $M_H=2M_W$, showing that the basic features of these solutions do not depend on the particular value of the Higgs mass (in this range of masses).

Starting from a given static neutral solution for a sphaleron-antisphaleron system characterized by the integers n and m, we have constructed the corresponding branch of rotating solutions, by slowly increasing the value of the parameter $\tilde{\gamma}=\gamma/g\upsilon$, which specifies the boundary conditions for the time components of the gauge fields.

The rotating branch ends when the limiting value $\tilde{\gamma}_{\rm max}=1/2$ is reached. In the asymptotic expansion, the exponential decay is determined by a decay constant proportional to $\sqrt{1-4\tilde{\gamma}^2}$. Beyond $\tilde{\gamma}_{\rm max}$ some of the gauge field functions would no longer decay exponentially, precluding localized solutions for larger values of $\tilde{\gamma}$. Consequently, at $\tilde{\gamma}_{\rm max}$ the respective solution has maximal angular momentum, maximal charge, and maximal energy.

We have used the linear relation (19) between the charge $\mathcal{Q}$ and the angular momentum J as a check of the accuracy of the solutions. According to this relation, we should obtain a single straight line, when exhibiting the charge versus the scaled angular momentum J/n.

We demonstrate this in Fig. 1 for the sets of solutions with $m=2$ and $m=6$ by exhibiting the charge parameter χ (which is proportional to the charge $\mathcal{Q}$) versus the scaled angular momentum J/n. We indeed observe sets of superimposed straight line segments. Since the charge parameter has been extracted from the asymptotic falloff of the $U(1)$ function a_1, whereas the angular momentum has been obtained from the volume integral of the angular momentum density T^t_{φ}, this agreement reflects the good numerical quality of the solutions.

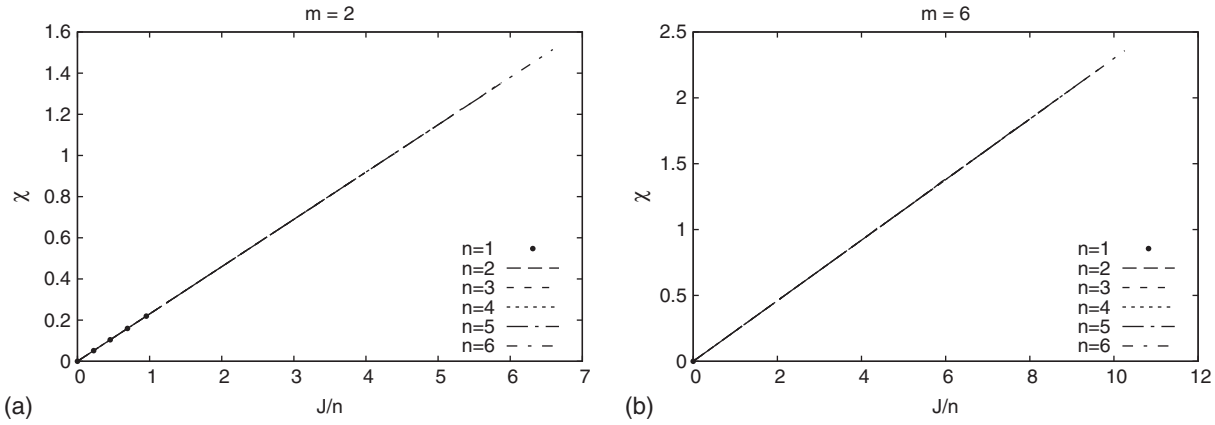

FIG. 1. Quality of the solution set: the charge parameter χ versus the scaled angular momentum J/n (in units of $J_0=4\pi/g^2$). (a) $m=2$, $n=1,\ldots,6$, and (b) $m=6$, $n=1,\ldots,6$.

B. Global properties

We first address the domain of existence of these solutions. For that purpose we exhibit in Fig. 2 the asymptotic gauge field parameter $\tilde{\gamma} = \gamma/g\upsilon$ versus the scaled angular momentum of the solutions J/n, which corresponds to the charge $\mathcal{Q}/e$ (choosing units of $J_0 = 4\pi/g^2$). As $\tilde{\gamma}$ increases from zero to its maximal value $\tilde{\gamma}_{\max} = 1/2$, the angular momentum increases monotonically. Consequently, the solutions have maximal angular momentum at $\tilde{\gamma}_{\max}$.

We observe that for fixed m the maximal value of the scaled angular momentum J/n (respectively, charge $\mathcal{Q}/e$) increases with n. Thus the value of the maximal angular momentum $J_{\max}$ increases faster than linearly with n. For $m = 1$ the solutions are multisphaleron solutions, with n sphalerons superimposed at the origin. We thus see that the

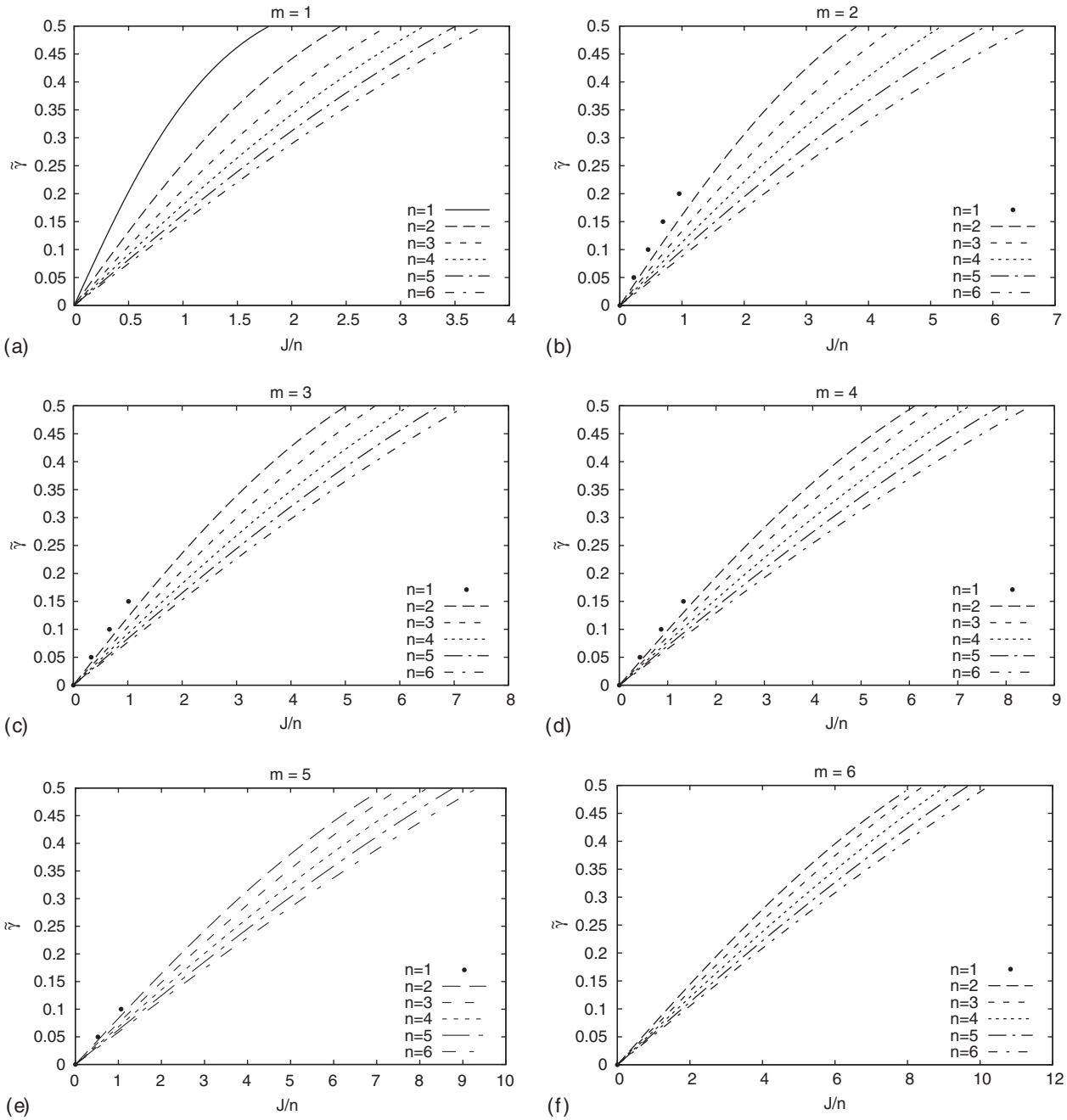

FIG. 2. Domain of existence of the solutions: the asymptotic value of the $U(1)$ field $\tilde{\gamma} = \gamma/g\upsilon$ versus the scaled angular momentum J/n (in units of $J_0 = 4\pi/g^2$). (a) $m = 1$, $n = 1, \ldots, 6$, (b) $m = 2$, $n = 1, \ldots, 6$, (c) $m = 3$, $n = 1, \ldots, 6$, (d) $m = 4$, $n = 1, \ldots, 6$, (e) $m = 5$, $n = 1, \ldots, 6$, and (f) $m = 6$, $n = 1, \ldots, 6$.

more sphalerons a configuration consists of, the more angular momentum the constituents can carry. We reach the analogous conclusion by considering a fixed value of n and varying m. The maximal value of the scaled angular momentum $J_{\max}/n$ increases with m. Thus the higher the number of constituents of a configuration (encoded in the product mn), the more angular momentum each of the constituents can carry.

We exhibit in Fig. 3 the energy of the sets of solutions. In Fig. 3(a) the energy of the multisphaleron solutions is shown. For multisphalerons consisting of n sphalerons, the energy is on the order of n times the energy of a single sphaleron; thus E/n is roughly constant. The deviations of the energy per sphaleron E/n from the energy of a single sphaleron can be attributed to the interaction of the n sphalerons and therefore be interpreted in terms of the binding energy of these multisphaleron configurations. For the employed value of the Higgs mass the static solutions with $n = 2$–4 represent bound states, since E/n is smaller than the energy of a single sphaleron,

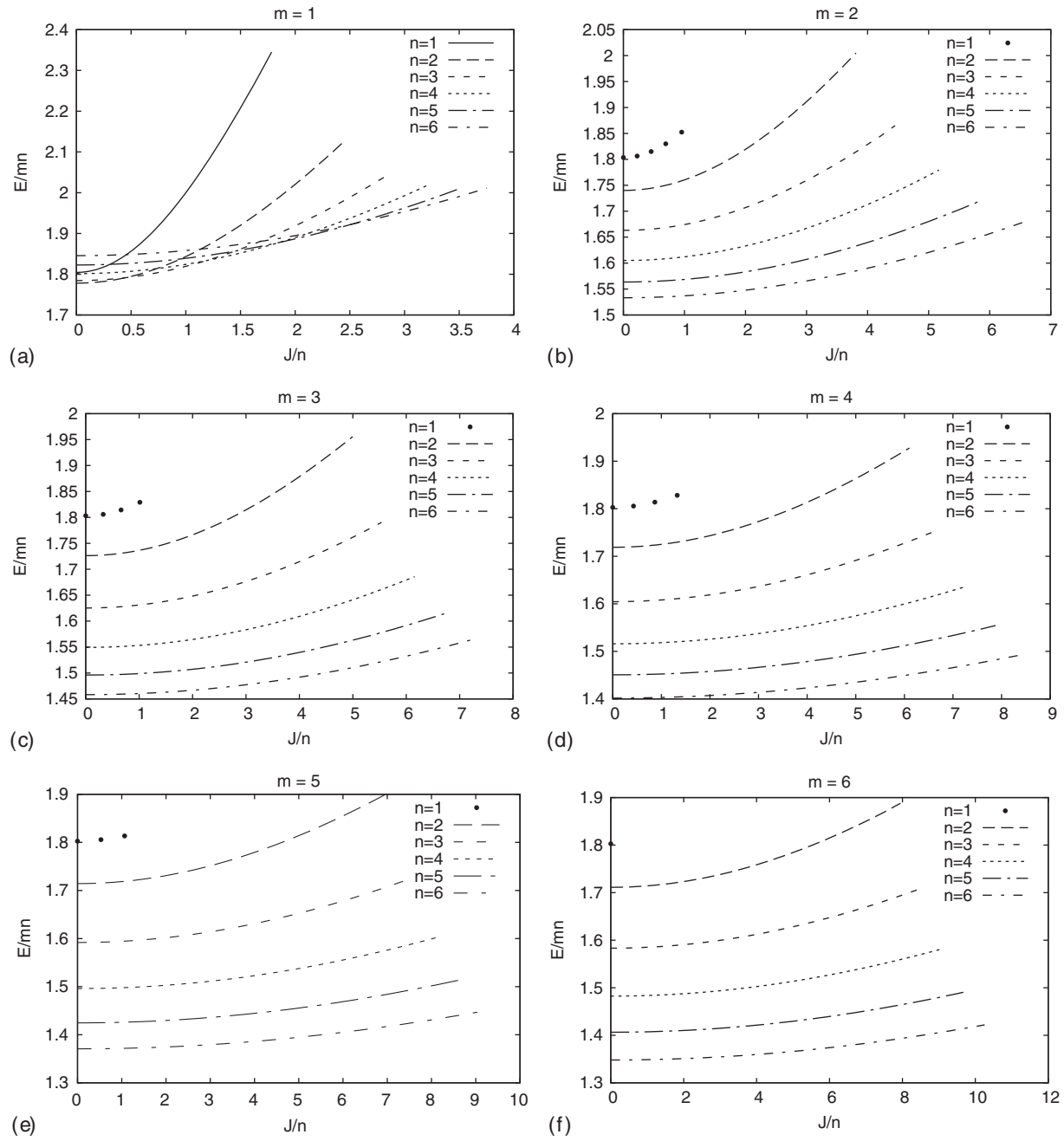

FIG. 3. Properties of the solutions: the scaled energy E/mn (in units of $E_0 = 4\pi v/g$) versus the scaled angular momentum J/n (in units of $J_0 = 4\pi/g^2$). (a) $m = 1$, $n = 1, \ldots, 6$, (b) $m = 2$, $n = 1, \ldots, 6$, (c) $m = 3$, $n = 1, \ldots, 6$, (d) $m = 4$, $n = 1, \ldots, 6$, (e) $m = 5$, $n = 1, \ldots, 6$, and (f) $m = 6$, $n = 1, \ldots, 6$.

whereas the static solutions with $n > 4$ are slightly unbound [17]. Since the binding energy is, however, sensitive to the value of the Higgs mass, bound configurations may turn into unbound configurations, when the value of the Higgs mass is sufficiently changed. When charge is added to these static multisphaleron configurations and the solutions begin to rotate, their energy increases monotonically with their angular momentum. The increase of the energy per sphaleron E/n with the angular momentum per sphaleron J/n is strongest for the branch of single sphaleron solutions. The more sphalerons a multisphaleron configuration consists of, the weaker is the increase of its energy per sphaleron E/n with increasing angular momentum per sphaleron J/n. Thus charge and rotation contribute relatively less to the total energy for these "many sphaleron" configurations (e.g. only 8% for $n = 6$ as compared to 30% for $n = 1$). Consequently, the rotating multisphaleron configurations turn into bound states beyond some critical value of the angular momentum.

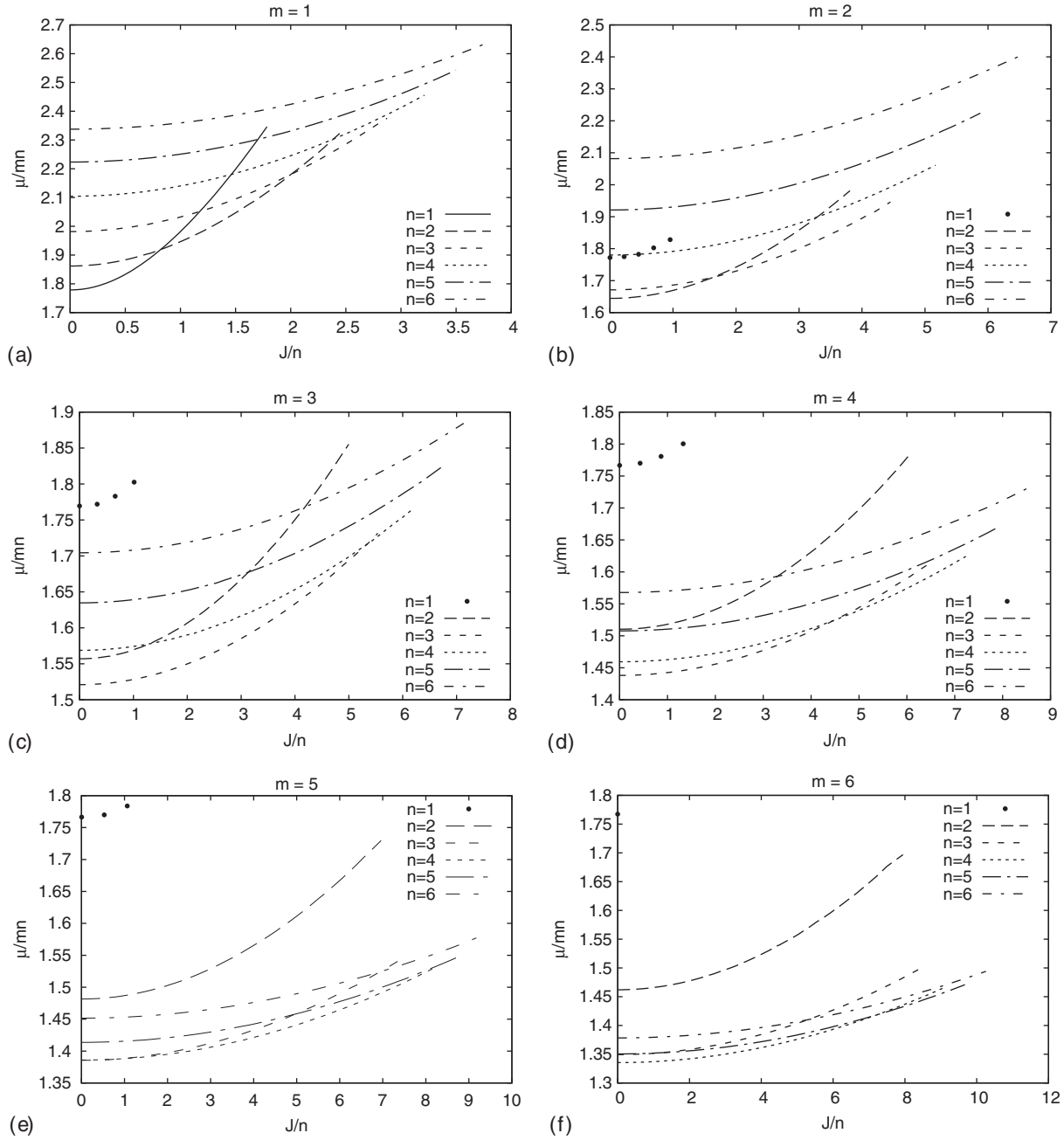

FIG. 4. Properties of the solutions: the scaled magnetic moment μ/n (in units of $\mu_0 = e/\alpha_W M_W$) versus the scaled angular momentum J/n (in units of $J_0 = 4\pi/g^2$). (a) $m = 1$, $n = 1, \ldots, 6$, (b) $m = 2$, $n = 1, \ldots, 6$, (c) $m = 3$, $n = 1, \ldots, 6$, (d) $m = 4$, $n = 1, \ldots, 6$, (e) $m = 5$, $n = 1, \ldots, 6$, and (f) $m = 6$, $n = 1, \ldots, 6$.

We next address the energy of the general sphaleron-antisphaleron systems, which we like to think of as consisting of the number mn of constituents. We therefore exhibit the scaled energy E/mn, i.e., the energy per constituent, in Figs. 3(b)–3(f). We see that for all $m > 1$ the energy per constituent E/mn is of the same order of magnitude. The deviations of E/mn from the energy of a single sphaleron are attributed to the interaction of the sphalerons and antisphalerons in the system (as long as these can be discerned) and can again be interpreted in terms of their binding energy. We note that the binding energy increases with an increasing number of constituents. Charge and rotation therefore contribute relatively less to the total energy in the ''many constituents'' configurations.

Finally, we exhibit in Fig. 4 the magnetic moment of the sets of solutions. Sphalerons possess a large magnetic moment μ. For multisphalerons consisting of n sphalerons, one expects from the superposition picture that the magnetic moment should be roughly n times the magnetic moment of a single sphaleron. As seen in Fig. 4(a), where we exhibit the magnetic moment per sphaleron μ/n of the multisphaleron configurations versus the angular momentum per sphaleron J/n, this guess is not that good for the static multisphalerons configurations. In fact, for these configurations the interaction between the sphalerons gives rise to an almost linear increase of the magnetic moment per sphaleron μ/n with the number of sphalerons. When charge, and thus angular momentum, is added to these multisphaleron configurations, their magnetic moment increases monotonically with increasing angular momentum. This increase is strongest for the branch of single sphaleron solutions, and the more sphalerons a configuration consists of, the weaker is the increase.

Addressing finally the magnetic moment μ of the sphaleron-antisphaleron systems, we exhibit in Figs. 4(b)–4(f) the magnetic moment per constituent μ/mn. Interestingly, for the chain configurations with $n = 1$, the magnetic moment per constituent μ/m is almost independent of m. However, generically the interaction between the constituents leads to a decrease of the magnetic moment per constituent μ/mn with increasing m.

C. Local properties

Having discussed the global properties of the sphaleron-antisphaleron systems, we now turn to their local properties. In particular, we address the effect of the presence of charge and rotation on the energy density $-T_t^t$, and on the modulus of the Higgs field $|\Phi|$. We also consider the angular momentum density T_φ^t and the component of the stress-energy density T_z^z, relevant for equilibrium.

In multisphalerons ($m = 1, n > 1$), the region with large energy density is toruslike and the maximum is forming a ring in the equatorial plane. When we add electric charge and angular momentum to the static configuration, we observe that the energy density is spreading further out, while at the same time its overall magnitude is reduced. Such a spreading of the energy density with increasing charge is also seen in dyons, for instance. We therefore attribute this effect to the presence of charge and the associated repulsion. Indeed, this spreading becomes quite pronounced for large values of the charge. The expected effect of the presence of angular momentum, on the other hand, is a centrifugal shift of the energy density. Indeed, we observe that with increasing angular momentum the toruslike region of large energy density moves further outward to larger values of ρ. These effects are seen in Fig. 5(a), where we exhibit the energy density $-T_t^t$ for a multisphaleron solution ($m = 1$, $n = 2$) in the static case ($\tilde{\gamma} = 0$) and for the almost maximally rotating case ($\tilde{\gamma} \approx 0.5$). In Figs. 5(b)–5(d) we also exhibit the magnitude of the Higgs field $|\Phi|$, the angular momentum density T_φ^t, and the stress-energy density component T_z^z for these two solutions.

The modulus of the Higgs field of the multisphaleron solutions has a single node at the origin, from where it starts to increase linearly in the direction of the symmetry axis, to reach its vacuum expectation value at infinity. In the equatorial plane, in contrast, the modulus of the Higgs field starts to increase from the origin much more slowly (i.e., only with power ρ^n). As the configurations are endowed with charge and rotation, the Higgs field changes only slightly. Indeed, the effect of charge and rotation on the modulus of the Higgs field is barely noticeable in Fig. 5(c) even at the maximal strength.

The angular momentum density for the multisphaleron solutions is toruslike and centered in the equatorial plane analogous to the energy density. However, the region of large angular momentum density is located further outwards at larger values of ρ, while it vanishes on the symmetry axis. The angular momentum density T_φ^t for the multisphaleron solution ($m = 1$, $n = 2$) for the maximally rotating case ($\gamma \approx 0.5$) is seen in Fig. 5(b).

Let us now turn to sphaleron-antisphaleron systems. For $n = 1$ they represent sphaleron-antisphaleron chains, where m sphalerons and antisphalerons are located on the symmetry axis, in static equilibrium. For $n = 2$ the chain is formed from m multisphalerons and multiantisphalerons; thus the modulus of the Higgs field still possesses only isolated nodes on the symmetry axis.

We demonstrate the effect of charge and rotation on these sphaleron-antisphaleron chains with $n = 2$, exhibiting the configurations with $m = 3$ and $m = 5$ in Figs. 6 and 7, respectively. Associated with each multisphaleron and multiantisphaleron is a toruslike part of the energy density. Thus a configuration with m multi(anti)sphalerons has m tori, located symmetrically with respect to the equatorial plane. As for the single multisphaleron, we observe that when we add electric charge and angular momentum to the

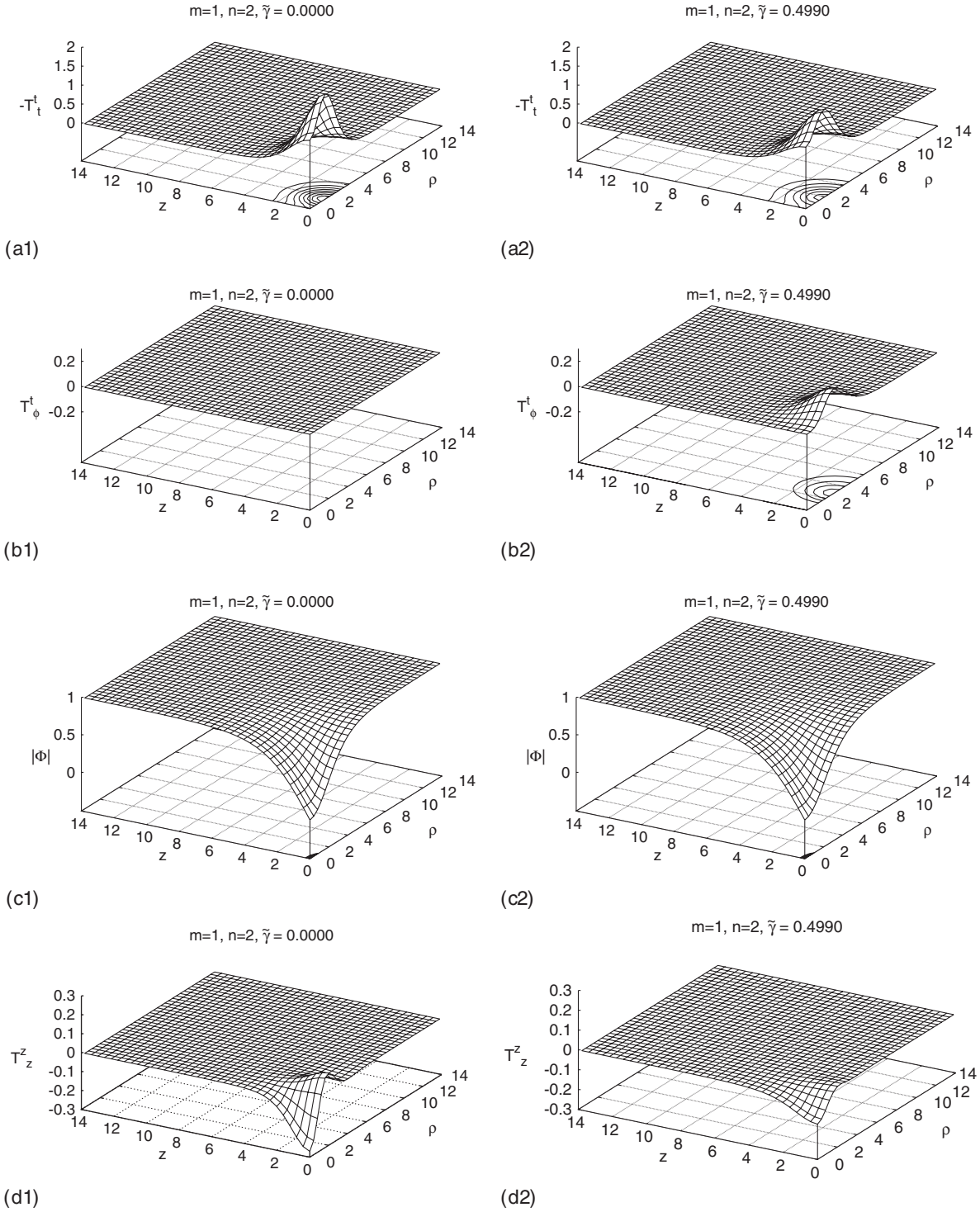

FIG. 5. The energy density $-T_t^t$ (a), the angular momentum density T_φ^t (b), the modulus of the Higgs field $|\Phi|$ (c), and the stress-energy density T_z^z (d) are exhibited for $m = 1$, $n = 2$ solutions with $\tilde{\gamma} = 0$ (left panels) and $\tilde{\gamma} \approx 0.5$ (right panels).

static configuration, the energy density is spreading further out, while its overall magnitude is reduced. Indeed, we observe that the toruslike regions of large energy density move further outward to larger values of ρ and further from each other to larger values of $|z|$. These effects are seen in Figs. 6(a) and 7(a). As clearly observable in Figs. 6(c) and 7(c), the nodes of the Higgs field move further apart, as the chains become charged and the rotation sets in.

Let us turn now to more complicated sphaleron-antisphaleron systems. As n increases beyond the value 2, the character of the solutions changes, and new types of configurations appear, where the modulus of the Higgs

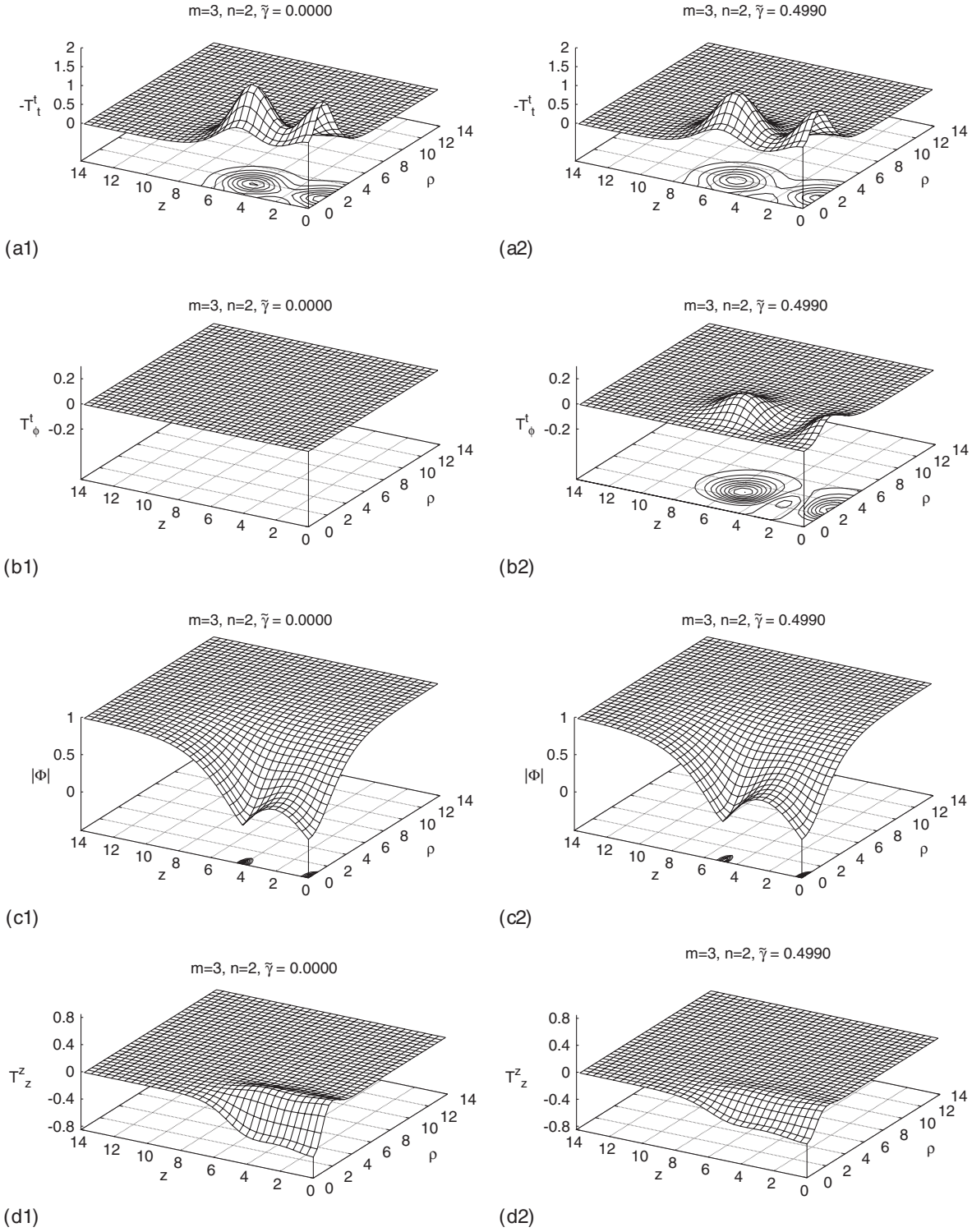

FIG. 6. The energy density $-T_t^t$ (a), the angular momentum density T_φ^t (b), the modulus of the Higgs field $|\Phi|$ (c), and the stress-energy density T_z^z (d) are exhibited for $m = 3$, $n = 2$ solutions with $\tilde{\gamma} = 0$ (left panels) and $\tilde{\gamma} \approx 0.5$ (right panels).

field vanishes on rings centered around the symmetry axis. Therefore, we refer to these solutions as vortex ring solutions. We note that the precise evolution of the isolated nodes on the symmetry axis and the vortex rings in the bulk with increasing n is somewhat sensitive to the value of the Higgs mass [22].

The nodes of the sphaleron-antisphaleron systems in the range $m = 2$–6 and $n = 3$–6 are exhibited in Fig. 8 for

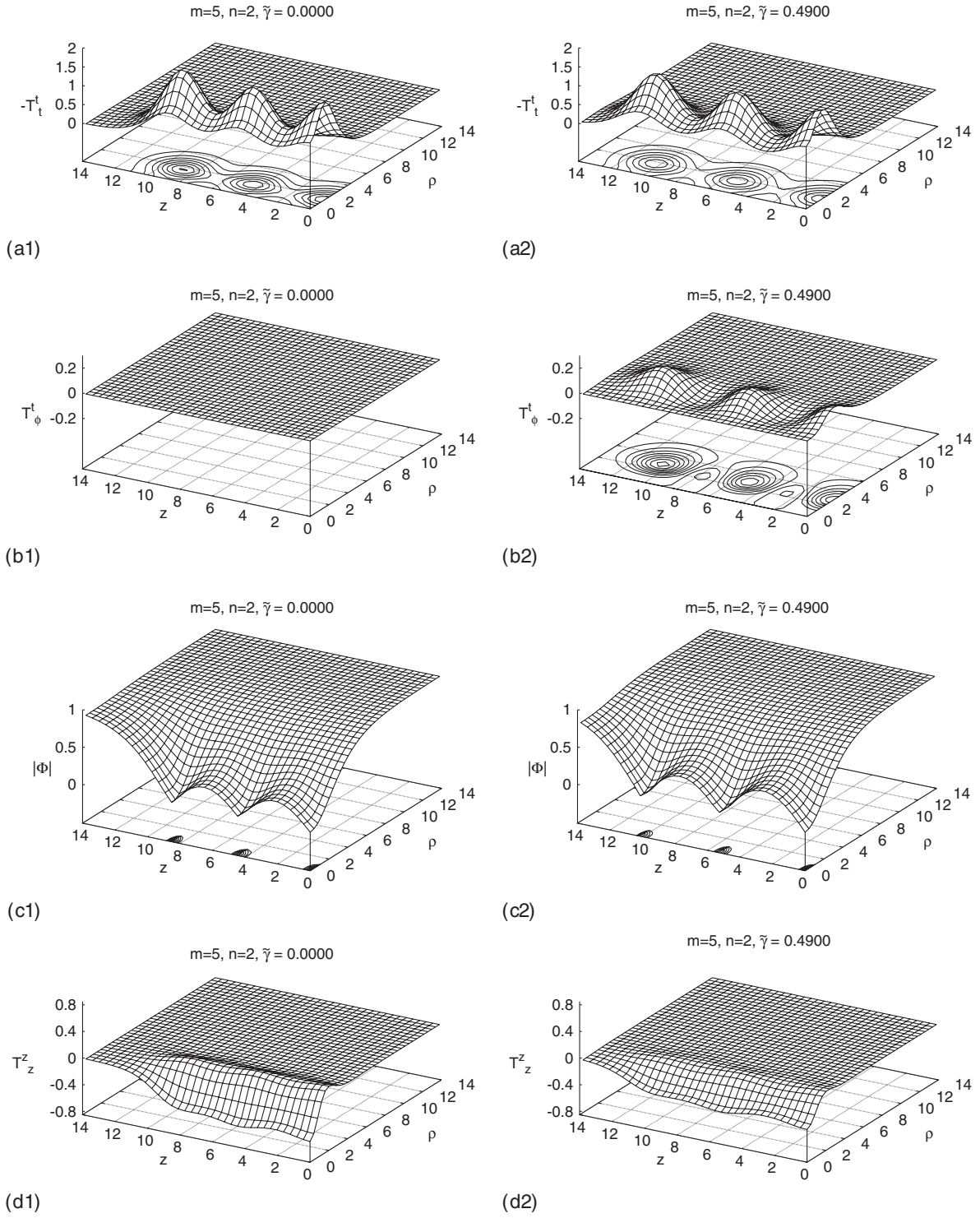

FIG. 7. The energy density $-T_t^t$ (a), the angular momentum density T_φ^t (b), the modulus of the Higgs field $|\Phi|$ (c), and the stress-energy density T_z^z (d) are exhibited for $m = 5$, $n = 2$ solutions with $\tilde{\gamma} = 0$ (left panels) and $\tilde{\gamma} \approx 0.5$ (right panels).

vanishing charge and rotation. For the chosen parameters, the modulus of the Higgs field of the simplest vortex ring configuration, i.e., the system with $m = 2$, $n = 3$, vanishes on a single ring located in the equatorial plane. As the winding number n increases, this single ring merely increases in size, as seen in the figure. For $n \geq 5$ this increase is, to a high degree, linear.

The $m = 3$, $n = 3$ configuration has one node at the origin and, in addition, two tiny rings, located symmetrically above and below the xy plane. As n increases, the

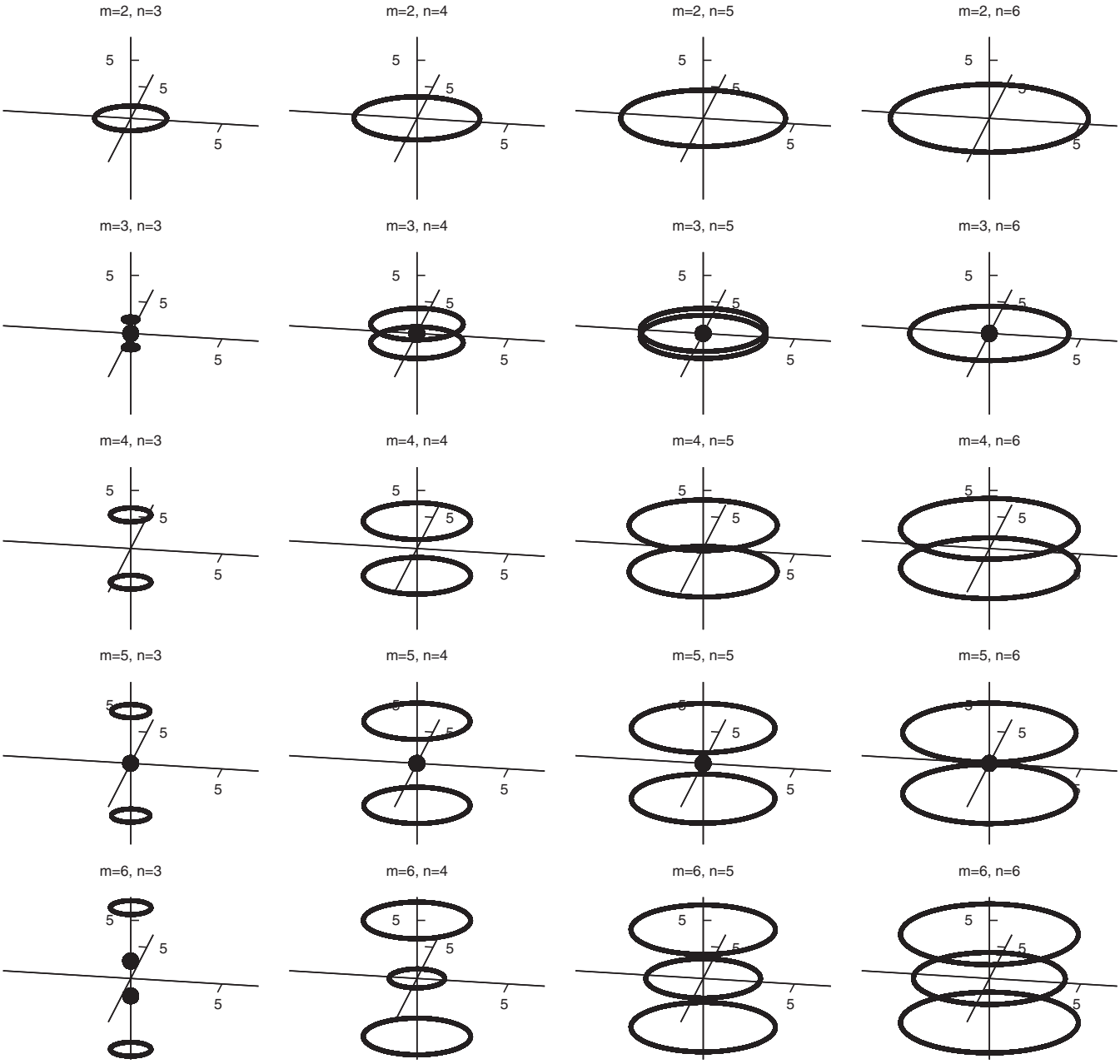

FIG. 8. The nodes of the Higgs field for the static sphaleron-antisphaleron systems with $m = 2$–6, $n = 3$–6. Rows show fixed m, while columns show fixed n.

rings grow in size and move towards each other. For $n = 6$ the rings have merged into a single ring in the equatorial plane. This ring then grows in size as n increases further, while the central node is always retained.

The static $m = 4$, $n = 3$ configuration has two vortex rings, located symmetrically with respect to the xy plane. While the rings increase in size with increasing n, they hardly change their mutual distance for intermediate values of n, as depicted in the figure. To see the further evolution of the nodes and be able to decide whether they merge into a single ring in the equatorial plane, we have continued the calculations up to $n = 72$. Here the rings are already rather close, but they have still not merged. Extrapolating the curve $z_{\mathrm{ring}}(n)$ indicates that a merging may happen only beyond $n = 100$.

For $m = 5$, $n = 3$ there are two symmetrically located vortex rings supplemented by a node at the origin. As n increases, the rings again increase in size, at first roughly retaining their distance. However, they slowly move towards each other and merge into a single ring at $n = 37$.

For $m = 6$, $n = 3$ there are two symmetrical vortex rings and two inner nodes on the symmetry axis. For $n = 4$ the inner nodes have already formed a ring in the

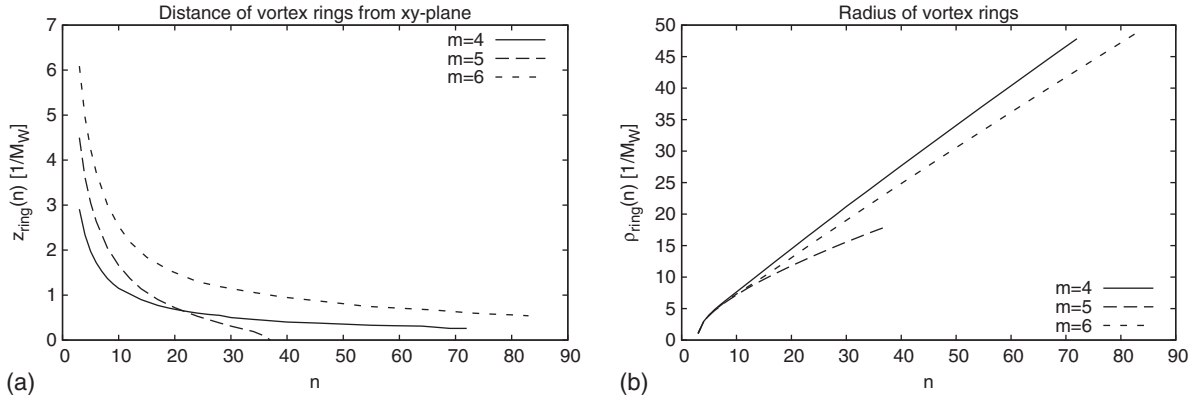

FIG. 9. Distance of vortex rings from the xy plane (a) and their radius (b) for $m = 4, 5, 6$, $\tilde{\gamma} = 0$, as a function of winding number n. The radius of the central ring of the $m = 6$ solutions is not shown.

equatorial plane. With increasing n all three rings then grow in size. For $n = 83$ the outer rings have come closer to the equatorial plane, but merging has not yet taken place. An extrapolation of $z_{\mathrm{ring}}(n)$ and $\rho_{\mathrm{ring}}(n)$ for the three rings shows that a merging of the rings will most likely not happen until n is well above 100. We display $z_{\mathrm{ring}}(n)$ and $\rho_{\mathrm{ring}}(n)$ in Fig. 9 for the solutions with $m = 4, 5, 6$.

In the following, we demonstrate the effect of charge and rotation on these sphaleron-antisphaleron systems. Concerning the location and type of nodes, we observe only a small effect. For $m = 2$, $n = 3$ the location of the rings changes by about 20%, between the static case and maximal rotation, but typically the changes are on the order of 10%. Only in the vicinity of transitions between the numbers and types of nodes, the effects of charge and rotation on the nodes become rather important.

Let us now illustrate our discussion of the effect of charge and rotation by considering the configurations $m = 6$ and $n = 3, 4, 5$. These are exhibited in Figs. 10–12, where we again display the energy density $-T_t^t$, the modulus of the Higgs field $|\Phi|$, the angular momentum density T_φ^t, and the stress-energy density component T_z^z for static solutions and solutions with maximal rotation.

In these sphaleron-antisphaleron systems, the regions with large energy density are toruslike, where the configurations possess six such tori. Their location depends on n and on the parameters. With increasing n these tori degenerate, basically forming a single cylinder. As before, the effect of the presence of electric charge is that the energy density spreads further out, while at the same time its overall magnitude reduces. Likewise, the effect of the presence of angular momentum is a centrifugal shift of the energy density. With increasing angular momentum the toruslike regions of large energy density move further outward to larger values of ρ.

The modulus of the Higgs field of the sphaleron-antisphaleron systems changes only slightly with increasing charge and angular momentum. Indeed the change is barely noticeable in these figures, even though the static systems are compared to those that carry maximal charge and angular momentum. We therefore address the effect on the nodes of the Higgs field separately in Fig. 13, where we exhibit for the system $m = 6$, $n = 5$ the modulus of the Higgs field in the equatorial plane with increasing charge parameter $\tilde{\gamma}$. The effect on the size of the ring is an increase of roughly 10% due to charge and rotation. For comparison, we also exhibit the modulus of the Higgs field on the z axis, choosing the system $m = 5$, $n = 2$, where the nodes are pointlike. Here we observe an increase of the distance between the nodes also on the order of 10% due to charge and rotation.

The angular momentum density of the sphaleron-antisphaleron systems is also characterized by the presence of tori. There are tori of large positive angular momentum density as well as negative angular momentum density. The tori of the angular momentum density are spatially related to the tori of the energy density. In particular, the location of the positive tori is associated with the location of the tori of the energy density, with the negative tori in between.

D. Equilibrium condition

Let us finally address the question of the equilibrium of such composite configurations as sphaleron-antisphaleron pairs and more general sphaleron-antisphaleron systems. As discussed previously [34–36], a necessary condition for the equilibrium of such axially symmetric configurations is

$$\int_S T_{zz} dS = 0, \tag{27}$$

where T_{zz} is the respective component of the stress-energy tensor and S is the equatorial plane. When this condition is satisfied, the net force between the constituents in the upper and in the lower hemisphere vanishes, thus yielding equilibrium. If T_{zz} vanishes everywhere in the equatorial plane, this condition is met trivially; if on the other hand, T_{zz} does not identically vanish, the various contributions to the surface integral (27) must precisely cancel each other.

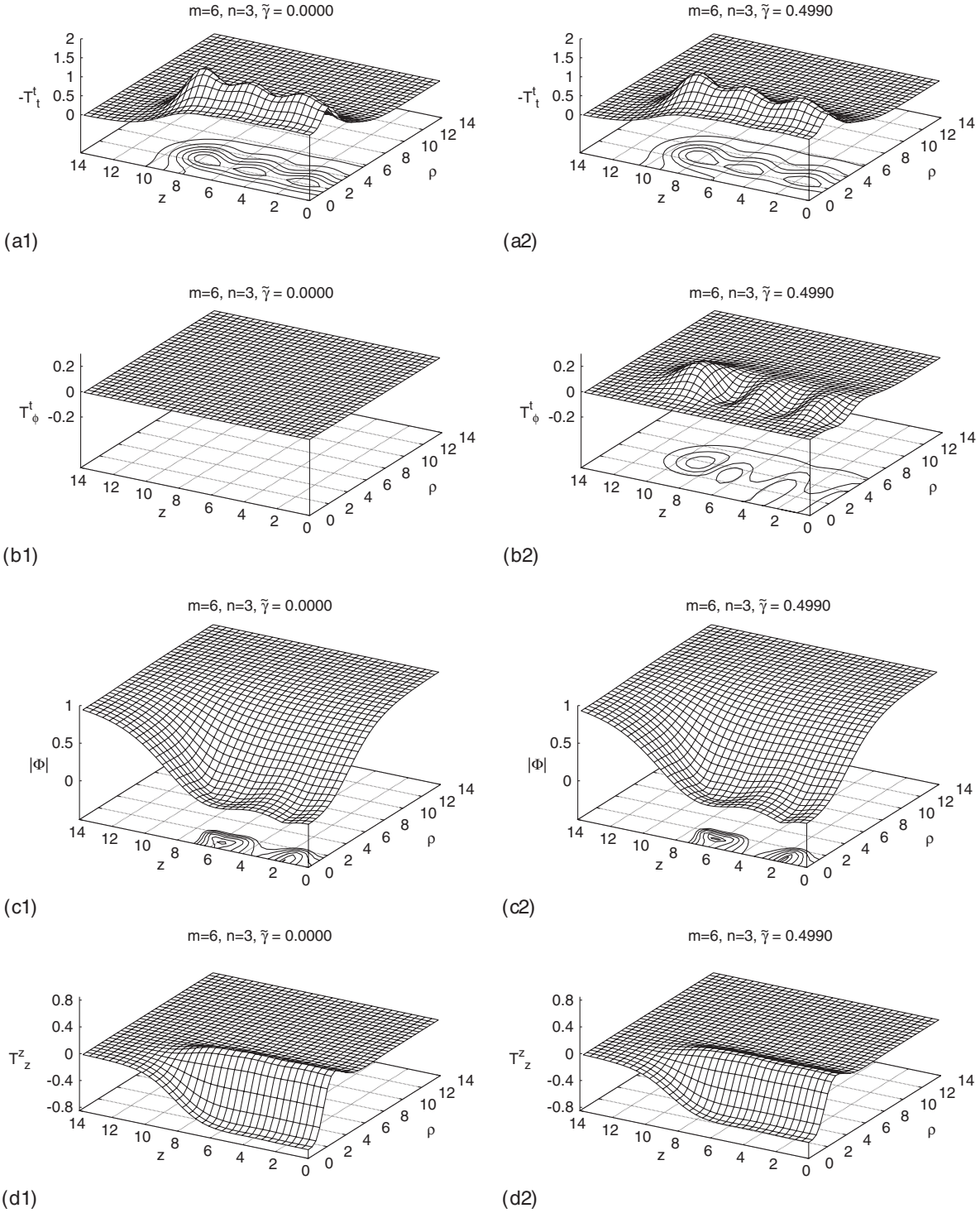

FIG. 10. The energy density $-T_t^t$ (a), the angular momentum density T_φ^t (b), the modulus of the Higgs field $|\Phi|$ (c), and the stress-energy density T_z^z (d) are exhibited for $m = 6$, $n = 3$ solutions with $\tilde{\gamma} = 0$ (left panels) and $\tilde{\gamma} \approx 0.5$ (right panels).

To understand how the equilibrium condition is satisfied in these sphaleron-antisphaleron systems, we have extracted the T_{zz} component of the stress-energy tensor. We illustrate T_{zz} for two rather different configurations in Fig. 14. In Fig. 14(a) we display T_{zz} for the static sphaleron-antisphaleron chain with $m = 4$, $n = 1$ in the upper hemisphere. In the equatorial plane T_{zz} appears to almost vanish. We therefore focus on the equatorial plane in Fig. 14(c). Here T_{zz} is small, but finite (except when it changes sign). To gain further insight into how the equilibrium results from the various forces present in the system, we consider the contributions from the respective

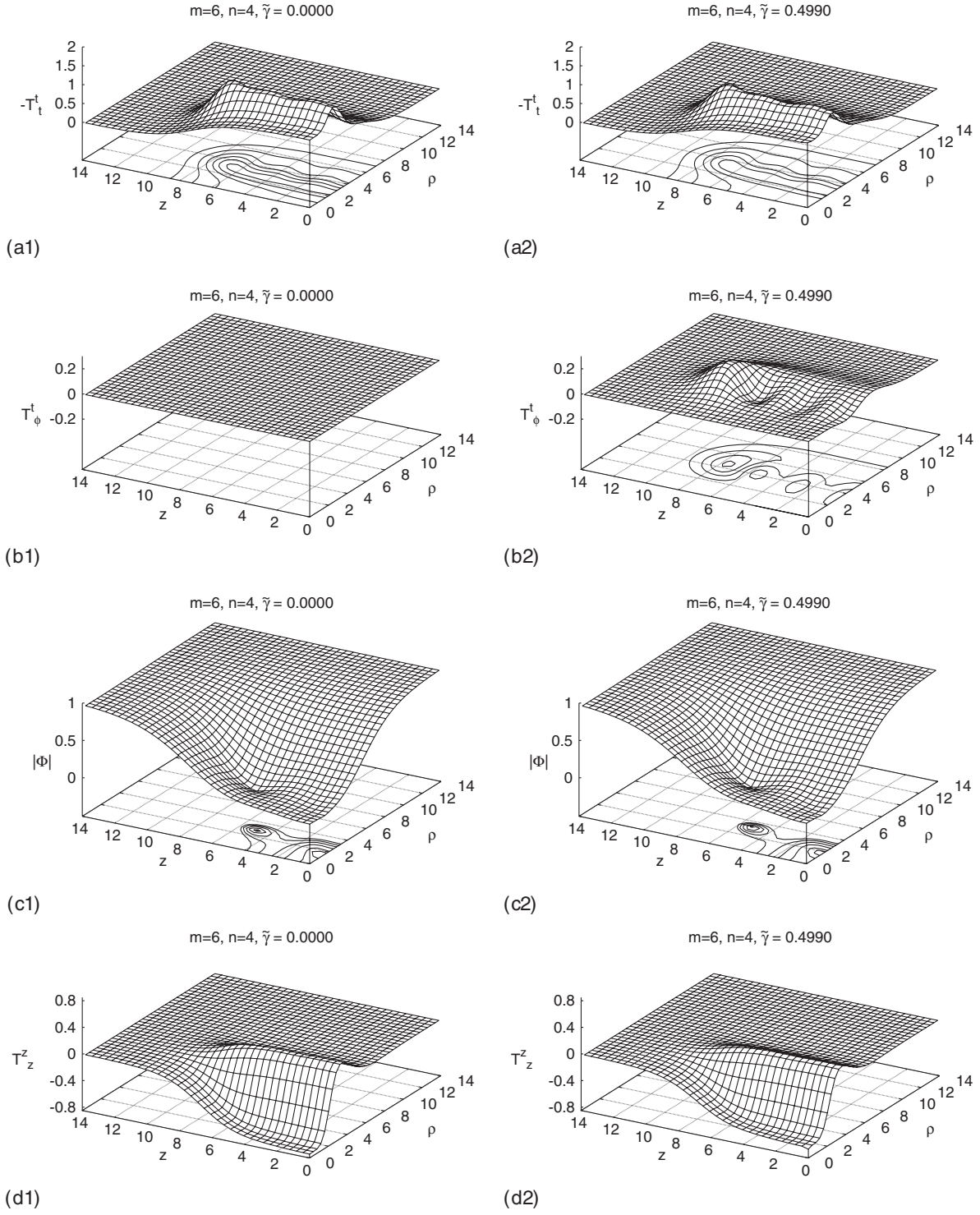

FIG. 11. The energy density $-T_t^t$ (a), the angular momentum density T_φ^t (b), the modulus of the Higgs field $|\Phi|$ (c), and the stress-energy density T_z^z (d) are exhibited for $m = 6$, $n = 4$ solutions with $\tilde{\gamma} = 0$ (left panels) and $\tilde{\gamma} \approx 0.5$ (right panels).

parts of the Lagrangian separately. We exhibit these also in Fig. 14(c). We note that the positive contribution from the $SU(2)$ gauge field part almost cancels the negative contributions from the $U(1)$ and Higgs parts, yielding, in total, a T_{zz} which is almost but not quite vanishing in the equatorial plane. In the inner region the total T_{zz} is slightly positive, while in the outer region it is slightly negative, yielding together a vanishing surface integral (27), within the numerical accuracy.

The situation is similar for other sphaleron-antisphaleron chains with even m and $n = 1$, including the sphaleron-antisphaleron pair. Also, the inclusion of rotation does not

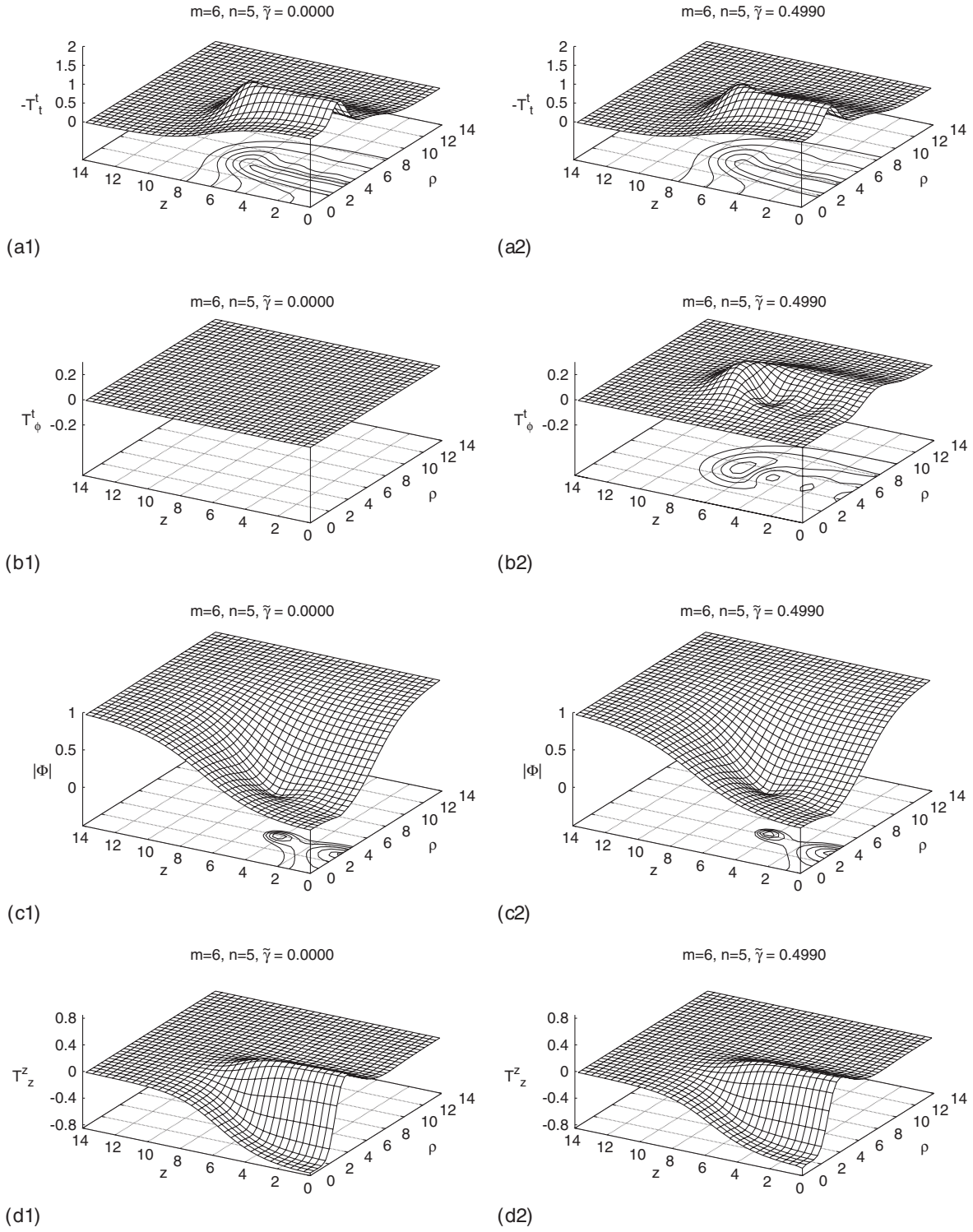

FIG. 12. The energy density $-T_t^t$ (a), the angular momentum density T_φ^t (b), the modulus of the Higgs field $|\Phi|$ (c), and the stress-energy density T_z^z (d) are exhibited for $m = 6$, $n = 5$ solutions with $\tilde{\gamma} = 0$ (left panels) and $\tilde{\gamma} \approx 0.5$ (right panels).

change this overall behavior of these types of solutions. For most other systems, however, T_{zz} does not nearly vanish in the equatorial plane. This is exhibited exemplarily in Fig. 14(b) for the fast rotating sphaleron-antisphaleron system with $m = 6$, $n = 5$. The features of T_{zz} seen here are very typical, and hardly change with rotation: the effect of rotation is basically a slight shift in magnitude. However, while T_{zz} is rather large in the equatorial plane for these configurations, its positive and negative contributions to the surface integral do cancel as required for equilibrium.

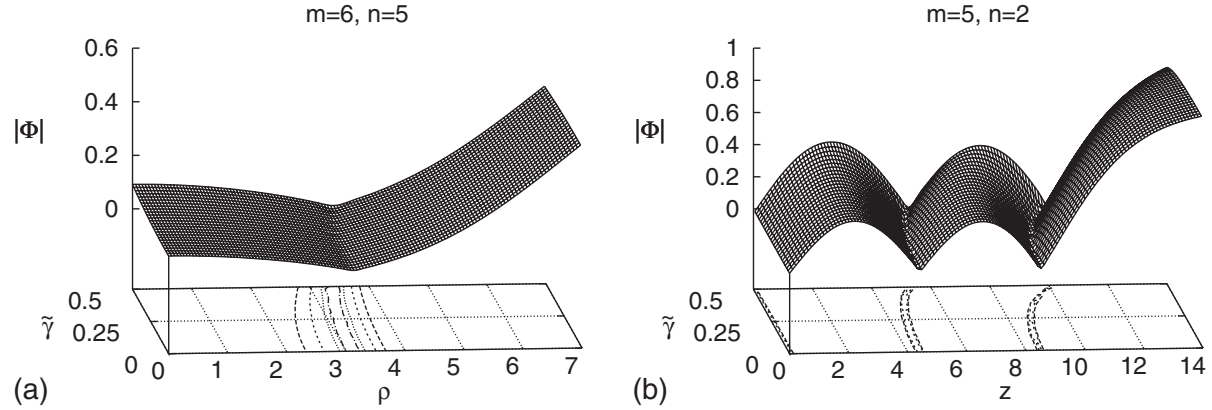

FIG. 13. The modulus of the Higgs field $|\Phi|$ versus the charge parameter $\tilde{\gamma}$ (a) in the equatorial plane for the vortex ring configuration $m = 6$, $n = 5$, and (b) on the z axis for the sphaleron-antisphaleron chain $m = 5$, $n = 2$.

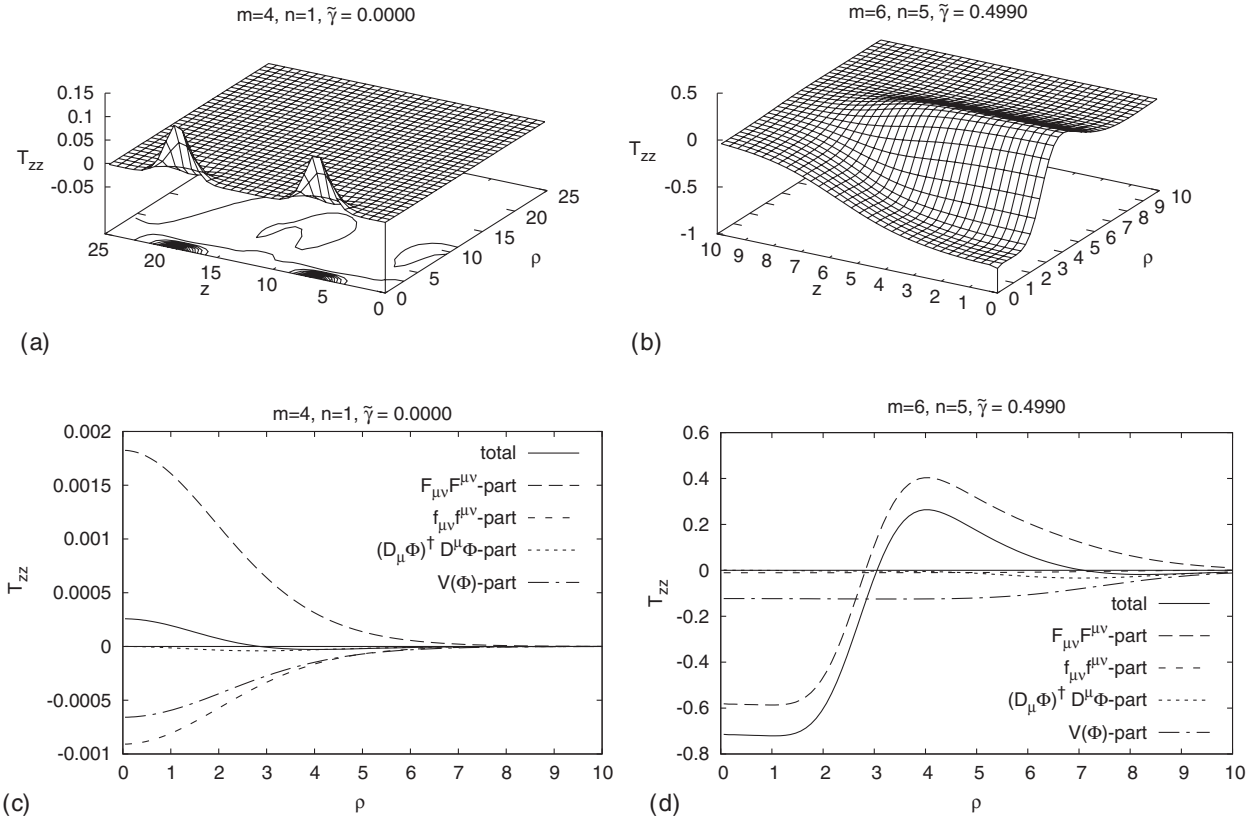

FIG. 14. The full stress-energy component T_{zz} (upper panels) and its $SU(2)$, $U(1)$, Higgs covariant derivative, and Higgs potential parts in the equatorial plane (lower panels) for the sphaleron-antisphaleron systems $m = 4$, $n = 1$, $J = 0$ (left panels) and $m = 6$, $n = 5$, $J \approx J_{\max}$ (right panels).

IV. CONCLUSIONS

We have considered sphaleron-antisphaleron pairs, chains, and vortex ring solutions in Weinberg-Salam theory, which are characterized by two integers, n and m. Starting from the respective neutral electroweak configurations, we have obtained the corresponding branches of rotating electrically charged solutions. These branches exist up to maximal values of the charge and angular momentum, beyond which localized solutions are no longer possible.

We have performed a complete study of all configurations with $m = 1$–6 and $n = 2$–6, fixing the weak mixing angle at its physical value and taking a fixed

value of the Higgs mass. The chain configurations with $m = 2$–6 and $n = 1$ have only partially been obtained with sufficiently high accuracy, to include their global properties such as their energy and magnetic moment into our systematic survey. For these chains our efforts are still continuing.

On the other hand, in order to clarify the evolution of the nodal structure of these sphaleron-antisphaleron systems, we have gone to rather high values of n, for static configurations, while extrapolating from the full study that the nodal structure is not much affected by the presence of charge and rotation. In particular, we have observed that the various rings in the vortex ring configurations tend to increase in size linearly with n, while at the same time tending to merge into a single ring in the equatorial plane. For $m = 3$ this merging transition occurs at $n = 6$, and for $m = 5$ at $n = 37$, while for the even m cases 4 and 6, a merging may occur only beyond $n = 100$.

The angular momentum J and the charge $\mathcal{Q}$ of these sphaleron-antisphaleron systems are proportional,

$$J = n\mathcal{Q}/e.$$

Their energy and binding energy increase with increasing rotation, and so does their magnetic moment. With increasing charge the energy density of the configurations spreads further out, while its overall magnitude reduces. At the same time, the effect of the rotation is a centrifugal shift of the energy density tori to larger radii.

We have also addressed the equilibrium condition (27) for these sphaleron-antisphaleron systems. In all systems, it is the surface integral that vanishes to give equilibrium, and not the stress-energy tensor component T_{zz} by itself. However, for the sphaleron-antisphaleron pair (and other even m chains) the stress-energy tensor component T_{zz} almost vanishes in the equatorial plane. In these configurations the positive contribution from the $SU(2)$ part almost cancels the negative contributions from the $U(1)$ and Higgs parts, thus yielding an almost vanishing total T_{zz} in the equatorial plane.

These configurations carry baryon number $Q_{\mathrm{B}} = (n(1 - (-1)^m))/4$; i.e., the baryon number vanishes for even m, while it is finite for odd m, independent of electric charge and rotation. We conjecture that for odd m noncontractible loops can be constructed, leading from a vacuum with vanishing baryon charge to a topologically distinct vacuum with charge $Q_{\mathrm{B}} = n$, passing a sphaleron-antisphaleron system configuration with $Q_{\mathrm{B}} = n/2$ midway.

We expect that at least some of the sphaleron-antisphaleron systems should persist at finite temperature, when temperature-dependent effective potentials are included, analogous to the case of the single sphaleron [37]. Then, at finite temperature, paths involving appropriate sphaleron-antisphaleron systems should allow for thermal fermion number violating transitions. While the energy of the configurations will be larger than that of the single static sphaleron, for low and intermediate values of m and n it should still be of the same order of magnitude. Thus some of the new configurations may offer alternative passages between the distinct vacua and consequently affect the rate of baryon and lepton number violating transitions.

The finite temperature paths involving appropriate sphaleron-antisphaleron systems may be compared to tunneling transitions via multi-instantons at zero temperature. Since multi-instantons with winding number n possess n fermion zero modes, we expect to encounter n fermion zero modes along vacuum to vacuum paths, passing a sphaleron-antisphaleron system configuration with $Q_{\mathrm{B}} = n/2$. Therefore, one of the next steps will be to study the fermion modes in the background of rotating electroweak configurations, furthering our understanding of their relevance for baryon number violating processes [38].

We also expect that the sphaleron-antisphaleron system configurations can be embedded in more elaborate models like the minimal supersymmetric extensions of the standard model. Calculation of these solutions is clearly another important step. Moreover, it will be interesting to include the effect of gravitation [39] to obtain rotating gravitating regular configurations as well as black hole solutions. Here a fascinating possibility would be the existence of a pair of black holes kept apart by the non-Abelian interactions between the sphaleron and antisphaleron configurations without the need for a conical singularity.

ACKNOWLEDGMENTS

We gratefully acknowledge discussions with Y. Brihaye and E. Radu. R. I. acknowledges support by the Volkswagen Foundation, and B. K. support by the DFG.

[1] G. 't Hooft, Phys. Rev. Lett. **37**, 8 (1976).
[2] A. Ringwald, Nucl. Phys. **B330**, 1 (1990).
[3] N. S. Manton, Phys. Rev. D **28**, 2019 (1983).
[4] F. R. Klinkhamer and N. S. Manton, Phys. Rev. D **30**, 2212 (1984).
[5] L. D. McLerran, Acta Phys. Pol. B **25**, 309 (1994).
[6] V. A. Rubakov and M. E. Shaposhnikov, Usp. Fiz. Nauk **166**, 493 (1996) [Phys. Usp. **39**, 461 (1996)].
[7] M. Dine and A. Kusenko, Rev. Mod. Phys. **76**, 1 (2003).

[8] F. R. Klinkhamer and C. Rupp, J. Math. Phys. (N.Y.) **44**, 3619 (2003).
[9] R. F. Dashen, B. Hasslacher, and A. Neveu, Phys. Rev. D **10**, 4138 (1974).
[10] J. Boguta, Phys. Rev. Lett. **50**, 148 (1983).
[11] B. Kleihaus, J. Kunz, and Y. Brihaye, Phys. Lett. B **273**, 100 (1991).
[12] J. Kunz, B. Kleihaus, and Y. Brihaye, Phys. Rev. D **46**, 3587 (1992).
[13] P. M. Saffin and E. J. Copeland, Phys. Rev. D **57**, 5064 (1998).
[14] E. Radu and M. S. Volkov, Phys. Rev. D **79**, 065021 (2009).
[15] B. Kleihaus, J. Kunz, and M. Leissner, Phys. Lett. B **678**, 313 (2009).
[16] B. Kleihaus and J. Kunz, Phys. Lett. B **329**, 61 (1994).
[17] B. Kleihaus and J. Kunz, Phys. Rev. D **50**, 5343 (1994).
[18] Y. Brihaye and J. Kunz, Phys. Rev. D **50**, 4175 (1994).
[19] F. R. Klinkhamer, Z. Phys. C **29**, 153 (1985).
[20] F. R. Klinkhamer, Phys. Lett. B **246**, 131 (1990).
[21] F. R. Klinkhamer, Nucl. Phys. **B410**, 343 (1993).
[22] B. Kleihaus, J. Kunz, and M. Leissner, Phys. Lett. B **663**, 438 (2008).
[23] B. Kleihaus, J. Kunz, and Y. Shnir, Phys. Lett. B **570**, 237 (2003).
[24] B. Kleihaus, J. Kunz, and Y. Shnir, Phys. Rev. D **68**, 101701 (2003).
[25] B. Kleihaus, J. Kunz, and Y. Shnir, Phys. Rev. D **70**, 065010 (2004).
[26] R. Ibadov, B. Kleihaus, J. Kunz, and M. Leissner, Phys. Lett. B **686**, 298 (2010).
[27] J. J. Van der Bij and E. Radu, Int. J. Mod. Phys. A **17**, 1477 (2002).
[28] B. Kleihaus, J. Kunz, and F. Navarro-Lerida, Phys. Rev. Lett. **90**, 171101 (2003).
[29] M. S. Volkov and E. Wohnert, Phys. Rev. D **67**, 105006 (2003).
[30] E. Radu and M. S. Volkov, Phys. Rep. **468**, 101 (2008).
[31] B. Kleihaus, J. Kunz, F. Navarro-Lerida, and U. Neemann, Gen. Relativ. Gravit. **40**, 1279 (2008).
[32] B. Kleihaus, J. Kunz, and K. Myklevoll, Phys. Lett. B **582**, 187 (2004).
[33] W. Schönauer and R. Weiß, J. Comput. Appl. Math. **27**, 279 (1989).
[34] Y. Aharonov, A. Casher, S. R. Coleman, and S. Nussinov, Phys. Rev. D **46**, 1877 (1992).
[35] R. Beig and R. M. Schoen, Classical Quantum Gravity **26**, 075014 (2009).
[36] R. Beig, G. W. Gibbons, and R. M. Schoen, Classical Quantum Gravity **26**, 225013 (2009).
[37] S. Braibant, Y. Brihaye, and J. Kunz, Int. J. Mod. Phys. A **8**, 5563 (1993).
[38] J. Kunz and Y. Brihaye, Phys. Lett. B **304**, 141 (1993).
[39] R. Ibadov, B. Kleihaus, J. Kunz, and M. Leissner, Phys. Lett. B **663**, 136 (2008).